

Influence of multiple scattering on three-dimensional imaging with optical diffraction tomography

Kamal Belkebir, Patrick C. Chaumet, and Anne Sentenac

Institut Fresnel (UMR 6133), Université d'Aix-Marseille I & III, Avenue Escadrille Normandie-Niemen, F-13397 Marseille cedex 20, France

Received May 3, 2005; revised July 8, 2005; accepted August 23, 2005

Optical diffraction tomography is an imaging technique that permits retrieval of the map of permittivity of an object from its scattered far field. Most reconstruction procedures assume that single scattering is dominant so that the scattered far field is linearly linked to the permittivity. In this work, we present a nonlinear inversion method and apply it to complex three-dimensional samples. We show that multiple scattering permits one to obtain a power of resolution beyond the classical limit imposed by the use of propagative incident and diffracted waves. Moreover, we stress that our imaging method is robust with respect to correlated and uncorrelated noise. © 2006 Optical Society of America
OCIS codes: 180.6900, 110.6960, 290.3200.

1. INTRODUCTION

In an optical diffraction tomography (ODT) experiment, the unknown object is illuminated under several angles of incidence and the diffracted field is collected along many directions of observation. In contrast to optical microscopy, in which lenses are used to image the object, ODT relies entirely on a numerical procedure to retrieve the three-dimensional map of permittivity of the sample. For a long time, this technique has been limited to the study of absorbing objects whose typical length scale is much larger than the wavelength. In the short-wavelength limit, the reconstruction algorithms are based on a geometrical model of propagation similar to techniques developed in x-ray tomography, and sole intensity measurements are necessary for retrieving the three-dimensional (3D) variations of the absorption in the sample. When the features of the object of interest are of the same order as the wavelength, the physical optics approximation is no longer valid and a more precise model of the electromagnetic scattering is necessary. In this case, most inverse procedures require amplitude and phase measurements. The latter can be obtained with a phase-shifting interferometry setup, as proposed by Lauer¹ or Destouches *et al.*²

The inversion procedures used in ODT experiments are usually based on the Rytov or the Born approximation under which the 3D Fourier components of the 3D scatterer are obtained from the two-dimensional (2D) Fourier components of the scattered field³ by varying the angle of the incident plane wave. The reconstruction of the map of permittivity is then performed with a simple Fourier transform. To compensate for the missing cones in the Fourier space due to the limited solid angle of collection and illumination and the discrete number of measures, reconstruction procedures using interpolation techniques, backpropagation algorithms, and least-squares minimizations have been developed.^{4,5} These methods are justified when there is a linear relationship between the scattered

field and the Fourier components of the permittivity, i.e., under the weak-scattering approximation.

Recently, a 3D linear inversion procedure based on the reconstruction of the induced currents in the object has been proposed to address imaging of objects with moderate dielectric contrast and size.⁶ Combined with an appropriate posttreatment, it leads to the resolution of two cubes of permittivity $\varepsilon = 2.25$ and of side $\lambda/4$ separated by $\lambda/4$ in the transverse plane, or $\lambda/2$ in the axial direction, with relatively few illumination and observation directions.

In this work, we consider the same experimental configuration, and we propose a nonlinear inversion scheme that takes into account the multiple-scattering effect. Although the presented inverse scheme does not use any regularization technique nor postprocessing procedure including prior information on the sample, it yields a higher resolution than that reached in the previous work of the authors.⁶ In Subsection 2.A, we sketch the coupled-dipole method that is used to simulate the experiment and in Subsection 2.B we describe the inversion procedure. In Section 3, we present several reconstructions from synthetic data and investigate the axial and transverse resolution and the role of multiple scattering. We analyze the sensitivity of the reconstruction to correlated and uncorrelated noise, and we point out the ability of our technique to image complex 3D objects. In Section 4 we present our conclusions.

2. THEORY

A. Formulation of the Forward-Scattering Problem

The coupled-dipole method (CDM) was introduced by Purcell and Pennypacker in 1973 for studying the scattering of light by nonspherical, dielectric grains in free space.⁷ The object under study is represented by a cubic array of N polarizable subunits. The monochromatic electromag-

netic field at each subunit can be expressed with the following self-consistent equation:

$$\mathbf{E}(\mathbf{r}_i) = \mathbf{E}^{\text{inc}}(\mathbf{r}_i) + \sum_{j=1, j \neq i}^N \vec{\mathbf{T}}(\mathbf{r}_i, \mathbf{r}_j) \alpha(\mathbf{r}_j) \mathbf{E}(\mathbf{r}_j), \quad (1)$$

where $\mathbf{E}^{\text{inc}}(\mathbf{r}_i)$ denotes the incident field at the position \mathbf{r}_i , i.e., the total electric field that would be observed in the absence of the scattering object. $\vec{\mathbf{T}}$ describes the linear response of a dipole in free space⁸ and $\alpha(\mathbf{r}_j)$ is the polarizability of the subunit j . According to the Clausius–Mossotti expression,⁹ the polarizability distribution α may be written as

$$\alpha(\mathbf{r}_j) = \frac{3d^3}{4\pi} \frac{\varepsilon(\mathbf{r}_j) - \varepsilon_0}{\varepsilon(\mathbf{r}_j) + 2\varepsilon_0}, \quad (2)$$

where d is the spacing of lattice discretization and $\varepsilon(\mathbf{r}_j)$ the relative permittivity of the object. The relative permittivity of the homogeneous background medium is denoted by ε_0 . This expression of the polarizability corresponds to the weak form of the CDM and is accurate enough for the present study. However, in a different topic, such as optical force analysis^{10–12} or extinction-cross-section modeling,¹³ one needs to take into account the radiative reaction term. The material under test is assumed to be isotropic. Hence, the relative permittivity $\varepsilon(\mathbf{r}_j)$ and subsequently the polarizability are both scalars.

Once Eq. (1) is solved, the scattered field $\mathbf{E}^{\text{d}}(\mathbf{r})$ at an arbitrary position \mathbf{r} exterior to the object is given by

$$\mathbf{E}^{\text{d}}(\mathbf{r}) = \sum_{j=1}^N \vec{\mathbf{T}}(\mathbf{r}, \mathbf{r}_j) \alpha(\mathbf{r}_j) \mathbf{E}(\mathbf{r}_j). \quad (3)$$

For the sake of simplicity Eq. (1) is rewritten in a more condensed form as

$$\mathbf{E} = \mathbf{E}^{\text{inc}} + \vec{\mathbf{A}}\mathbf{p}, \quad (4)$$

where $\vec{\mathbf{A}}$ is a square matrix of size $3N \times 3N$ and contains all the field susceptibilities $\vec{\mathbf{T}}(\mathbf{r}_i, \mathbf{r}_j)$. Further

$$\mathbf{E} = [E_x(\mathbf{r}_1), E_y(\mathbf{r}_1), E_z(\mathbf{r}_1), \dots, E_z(\mathbf{r}_N)],$$

$$\mathbf{E}^{\text{inc}} = [E_x^{\text{inc}}(\mathbf{r}_1), E_y^{\text{inc}}(\mathbf{r}_1), E_z^{\text{inc}}(\mathbf{r}_1), \dots, E_z^{\text{inc}}(\mathbf{r}_N)],$$

$$\mathbf{p} = [p_x(\mathbf{r}_1), p_y(\mathbf{r}_1), p_z(\mathbf{r}_1), \dots, p_z(\mathbf{r}_N)],$$

where \mathbf{E} and \mathbf{E}^{inc} denote the total and the incident electric field, respectively. The dipole moment \mathbf{p} is related to the electric field as $\mathbf{p}(\mathbf{r}_j) = \alpha(\mathbf{r}_j) \mathbf{E}(\mathbf{r}_j)$.

In an ODT experiment, the scattered field is collected at M observation points for L successive illuminations. Let \mathbf{E}_l^{d} be the scattered field corresponding to the l th illumination. We can then rewrite the far-field Eq. (3) in the condensed form

$$\mathbf{E}_l^{\text{d}} = \vec{\mathbf{B}}\mathbf{p}_l, \quad (5)$$

where $l=1, \dots, L$, and $\vec{\mathbf{B}}$ is a matrix of size $3M \times 3N$. The matrix $\vec{\mathbf{B}}$ contains the field susceptibilities $\vec{\mathbf{T}}(\mathbf{r}_k, \mathbf{r}_j)$, where \mathbf{r}_j denotes a point in the discretized object with $j=1, \dots, N$, while \mathbf{r}_k is an observation point with $k=1, \dots, M$. Note that $\vec{\mathbf{B}}$ does not depend on the angle of incidence.

B. Formulation of the Inverse-Scattering Problem

The geometry of the problem investigated in this paper is illustrated in Fig. 1. We assume that an unknown 3D object is entirely confined in a bounded box $\Omega \subset \mathbb{R}^3$ (test domain or an investigating domain) and illuminated successively by $l=1, \dots, L$ electromagnetic excitations $\mathbf{E}_{l=1, \dots, L}^{\text{inc}}$. For each excitation l , the scattered field \mathbf{f}_l is measured at M points on a surface Γ that is located outside the investigating domain Ω .

The inverse-scattering problem is stated as finding the permittivity distribution ϵ inside the investigation domain Ω such that the associated scattered field matches the measured field $\mathbf{f}_{l=1, \dots, L}$. Many accurate iterative techniques have been developed to solve this inverse problem. In these methods, starting from an initial guess, one adjusts the parameter of interest gradually by minimizing a cost functional involving the measured scattered-field data. Two main approaches can be found in the literature. In the first one,^{14–17} the linearized method, the field in the test domain Ω is considered fixed. This field is the solution of the forward problem—the solution of Eq. (4)—for the best available estimation of the permittivity at each iteration step, or it is the reference field if the Born approximation is assumed.

In the second approach,^{18,19} typically the modified gradient method, the field inside the test domain Ω is an un-

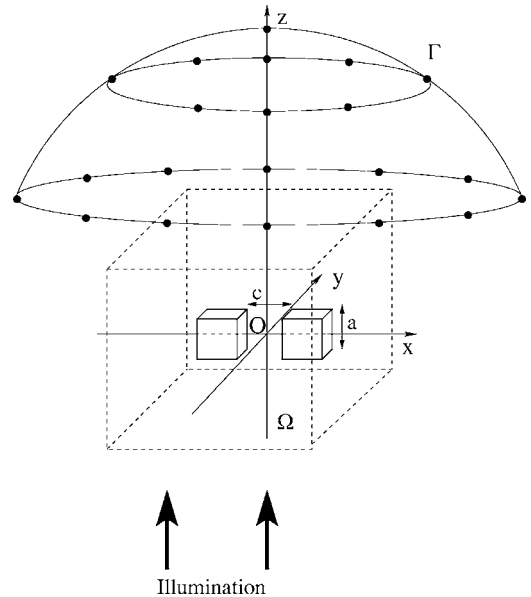


Fig. 1. Sketch of the illumination and detection configuration of the ODT experiment. The observation points are regularly placed on the half-sphere Γ (with a radius of 400λ). The illumination is as represented by the arrows, which denote a plane wave propagating toward positive z . For the ODT experiments, the authors took as illumination 16 plane waves in both planes (x, z) and (y, z) . The angle between the incident wave vector and the z axis ranges over -80° to 80° . See text for more detail.

known that is obtained, together with the permittivity, by the minimization procedure. A hybrid method^{20–22} that combines the ideas from the two approaches has also been developed. All these methods deal with 2D inverse-scattering problems. In three dimensions, most techniques use a linear inversion based on the Born approximation^{4,23} and are restricted to the scalar case.

Recently, a more advanced method, namely the contrast-source-inversion (CSI) method,²⁴ has been introduced for solving the full vectorial 3D problem.^{25,26} In the CSI method the induced dipoles are reconstructed iteratively by minimizing at each iteration step a cost functional involving both far-field Eq. (5) and domain-field Eq. (4). Here, we also present an iterative approach to solving this nonlinear and ill-posed inverse-scattering problem in which at each iteration step the forward problem, Eq. (4), is solved for the available estimation of the polarizability α . Thus, the field inside the test domain Ω is considered fixed at each iteration step. The sequence $\{\alpha_n\}$ is built up according to the recursive relation

$$\alpha_n = \alpha_{n-1} + a_n d_n, \quad (6)$$

where the updated polarizability α_n is deduced from the previous one α_{n-1} by adding a correction. This correction is composed of two terms: a scalar weight a_n and a search direction d_n . Once the updating direction d_n is found (this will be specified below), the scalar weight a_n is determined by minimizing the cost functional $\mathcal{F}_n(\alpha_n)$ involving the residual error $\mathbf{h}_{l,n}$ on the scattered field computed from observation Eq. (5),

$$\mathbf{h}_{l,n} = \mathbf{f}_l - \bar{\mathbf{B}} \alpha_n \mathbf{E}_l, \quad (7)$$

with \mathbf{E}_l being the total electric field that would be present in Ω if the polarizability distribution were α . This field can be written symbolically from Eq. (4) as

$$\mathbf{E}_l = [\bar{\mathbf{I}} - \bar{\mathbf{A}} \alpha]^{-1} \mathbf{E}_l^{\text{inc}}, \quad (8)$$

with $\bar{\mathbf{I}}$ being the identity matrix.

The cost functional $\mathcal{F}_n(\alpha_n)$ mentioned above reads as

$$\mathcal{F}_n(\alpha_n) = \frac{\sum_{l=1}^L \|\mathbf{h}_{l,n}\|_{\Gamma}^2}{\sum_{l=1}^L \|\mathbf{f}_l\|_{\Gamma}^2} = W_{\Gamma} \sum_{l=1}^L \|\mathbf{h}_{l,n}\|_{\Gamma}^2, \quad (9)$$

where the subscript Γ is included in the norm. $\|\cdot\|$ and later the inner product $\langle \cdot | \cdot \rangle$ in L^2 to indicate the domain of integration.

Note that substituting the expression of the polarizability α_n derived from Eq. (6) in Eq. (9) and approximating the actual field \mathbf{E}_l by the field that would be present in the investigating domain Ω for the best available estimate of the polarizability α , i.e.,

$$\mathbf{E}_l \approx \mathbf{E}_{l,n-1} = [\bar{\mathbf{I}} - \bar{\mathbf{A}} \alpha_{n-1}]^{-1} \mathbf{E}_l^{\text{inc}},$$

leads to a polynomial expression with respect to the scalar coefficient a_n . Thus the minimization of the cost functional $\mathcal{F}_n(\alpha_n)$ is reduced to a minimization of a simple cost function $\mathcal{F}_n(a_n)$. Moreover, for the particular case of dielectric material, i.e., the polarizability α is real, the cost function $\mathcal{F}_n(a_n)$ takes the form

$$\begin{aligned} \mathcal{F}_n(a_n) = W_{\Gamma} \sum_{l=1}^L (\|\mathbf{h}_{l,n-1}\|_{\Gamma}^2 + a_n^2 \|\bar{\mathbf{B}} d_n \mathbf{E}_{l,n-1}\|_{\Gamma}^2 \\ - 2a_n \text{Re} \langle \mathbf{h}_{l,n-1} | \bar{\mathbf{B}} d_n \mathbf{E}_{l,n-1} \rangle_{\Gamma}). \end{aligned} \quad (10)$$

In this case, the unique minimum of $\mathcal{F}_n(a_n)$ is reached for

$$a_n = \frac{\sum_{l=1}^L \text{Re} \langle \mathbf{h}_{l,n-1} | \bar{\mathbf{B}} d_n \mathbf{E}_{l,n-1} \rangle_{\Gamma}}{\sum_{l=1}^L \|\bar{\mathbf{B}} d_n \mathbf{E}_{l,n-1}\|_{\Gamma}^2}. \quad (11)$$

As updating direction d_n , the authors take

$$d_n = g_{n;\alpha} + \gamma_n d_{n-1}, \quad (12)$$

where g_n is the gradient of the cost functional \mathcal{F}_n with respect to the polarizability assuming that the total fields \mathbf{E}_l do not change:

$$g_{n;\alpha} = -W_{\Gamma} \sum_{l=1}^L \mathbf{E}_{l,n-1}^* \cdot \bar{\mathbf{B}}^{\dagger} \mathbf{h}_{l,n-1}, \quad (13)$$

in which \mathbf{u}^* denotes the complex conjugate of \mathbf{u} and $\bar{\mathbf{B}}^{\dagger}$ represents the transposed complex conjugate matrix of the matrix $\bar{\mathbf{B}}$.

The scalar coefficient γ_n is defined as in the Polak–Ribière conjugate-gradient method²⁷ by

$$\gamma_n = \frac{\langle g_{n;\alpha} | g_{n;\alpha} - g_{n-1;\alpha} \rangle_{\Gamma}}{\|g_{n-1;\alpha}\|_{\Gamma}^2}. \quad (14)$$

To complete the inverse scheme, we need to specify the initial guess. As initial estimate for α_0 the authors take the estimate obtained by the back-propagation procedure. This technique is described in detail for the 2D problem in Refs. 21 and 28–30. The extension to the 3D problem is straightforward and therefore does not need to be presented here.

3. NUMERICAL RESULTS

In this section we report some examples of reconstruction of targets from synthetic data for different configurations simulating ODT experiments. In all examples, the synthetic data were computed using the CDM in which the mesh size $\lambda/20$ of the scattering domain Ω is different from that used in the inversion $\lambda/10$, where λ stands for the wavelength of the incident field in the background medium. The scattered fields are evaluated at 65 points regularly distributed on half-sphere Γ (see Fig. 1). The radius of the sphere is 400λ so that only far-field component data are considered and the diffracted field at the observation point can be considered a plane wave with wave vector \mathbf{k}_d . The azimuthal angle of observation, defined as the angle between the diffracted wave vector and the z axis, ranges from $\theta = -80^\circ$ to 80° . The incident fields con-

sist of 16 plane waves. Eight plane waves have their wave vector \mathbf{k} and their electric field in the (x, z) plane (which corresponds to the p polarization), while the others have their wave vector and field in the (y, z) plane. The angle of incidence, defined as the angle between the incident wave vector and the z axis, varies from $\theta^{\text{inc}} = -80^\circ$ to 80° . In all the reconstructions, the investigation domain is a box of side 1.6λ surrounding the object, except in Figs. 9 and 10 below where the side of Ω is 2λ . The reconstructed permittivity is plotted after enough iterations for the cost function to reach a plateau.

A. Image of a Single Scatterer; Role of Multiple Scattering

In most imaging techniques in optics, such as far-field or near-field microscopes, the resolution is obtained by studying the “impulsional response” of the system, i.e., the image of a dipole (namely, a sphere or cube small enough that the electromagnetic field can be assumed to be constant over its volume). The latter is a function of the three variables of space, called the point-spread function (PSF). It presents a peak at the dipole position whose width at midheight along the x, y, z axis is commonly used to determine the transverse and axial power of resolution of the imaging technique. In a standard optical microscope in transmission, the width of the PSF is roughly $0.6\lambda/\text{NA}$ transversally and $2n\lambda/(\text{NA})^2$ axially, where $\text{NA} = n \sin \varphi$ is the numerical aperture of the system, n being the index of the propagation medium and φ being the half-aperture of the imaging optics-objective.

Defining the resolution of an imaging system from its response to a point source is relevant if one can assume that the image of a collection of dipoles is the convolution of the PSF with the dipole distribution. While this assumption is clearly justified in fluorescence microscopy, in which the sources radiate incoherently, it can be questioned in coherent microscopy or tomography, especially when multiple scattering is present.

To point out this difficulty, we have studied the image of a cube of width $\lambda/20$ and permittivity $\varepsilon = 2.25$ as obtained with the nonlinear inversion scheme. Because of its small width and moderate permittivity, the object can

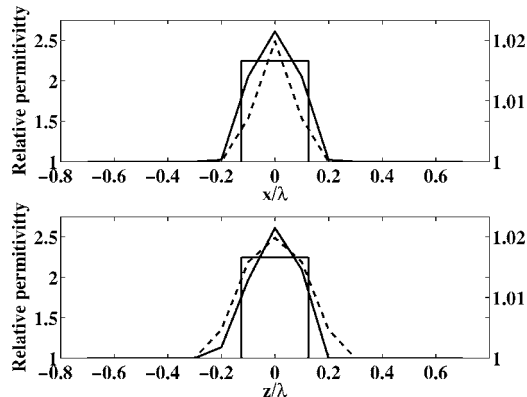


Fig. 2. Reconstructed permittivity of a single cube of permittivity $\varepsilon = 2.25$ of widths $\lambda/20$ (dashed curve) and $\lambda/4$ (solid curve). Upper figure, plot of the relative permittivity along the x axis; lower figure, plot along the z axis. The legend on the left is for the solid curve (large cube), on the right for the dashed curve (small cube).

be assimilated to a radiating dipole and its image can be considered as the PSF of our system. In Fig. 2 we compare the reconstructed permittivity of the dipole along the x and z axis to that of a cube of width $\lambda/4$ and same permittivity. The most important feature of Fig. 2 is that the width of the permittivity peak of the larger cube along the z axis is smaller than that of the dipole.

To confirm this surprising result, we have applied our nonlinear inversion scheme to two dipoles whose centers are separated by 0.6λ , and we compare the reconstructed map of permittivity to that of two cubes of width $\lambda/4$ whose centers are separated by the same distance. In Fig. 3(a) we display a map of the reconstructed permittivity of the dipoles while in Fig. 3(b) we plot the normalized reconstructed permittivity contrast $(\varepsilon - 1)/\max(\varepsilon - 1)$ along the z axis for the two dipoles and the two cubes. We observe that the two dipoles are not resolved while the cubes are easily distinguished. In our opinion, the presence of multiple scattering and the use of a nonlinear inversion scheme is responsible for the better resolution of the image of the two cubes. This observation calls in question the notion of resolution as usually defined by the PSF and it points up the difficulty of defining it in a nonlinear imaging system.

One can get a physical insight into the role of multiple scattering with the following arguments. Consider an object defined by its permittivity contrast with the background medium (vacuum), $\Delta\varepsilon(\mathbf{r}) = \varepsilon(\mathbf{r}) - 1$. The object is illuminated by a plane wave with wave vector \mathbf{k} . The far field diffracted along the direction defined by the wavevector \mathbf{k}_d can be assimilated to a plane wave with amplitude $\mathbf{E}(\mathbf{k}_d, \mathbf{k})$. Assuming the Born approximation, the latter is proportional to $\tilde{\Delta\varepsilon}(\mathbf{k}_d - \mathbf{k})$ where $\tilde{\Delta\varepsilon}$ is the 3D Fourier transform of $\Delta\varepsilon$.³¹ Hence, under the single-scattering approximation, the far-field amplitudes are directly linked to the Fourier transform of the permittivity contrast. By studying the spatial frequency domain, or the portion of the Ewald sphere that is covered by the experiment, one can estimate the limit of the resolution of the imaging system. In our configuration, the boundaries of the accessible spatial frequencies are roughly $[-2k_0, 2k_0]$ in the (x, y) plane and $[-k_0, k_0]$ along the z axis. Consequently, the expected widths at midheight of the dipole image are about $\lambda/4$ along the x axis and $\lambda/2$ along the z axis. The better result observed in Fig. 2 is due to the *a priori* information of the location of the dipole in a relatively small investigation box.⁶ Note that the PSF of a tomography experiment is naturally smaller than that of a microscope with the same NA ¹ because of the use of multiple illuminations.

When multiple scattering is present, the classical Fourier analysis no longer holds. Indeed, in this case, the amplitude of the far field diffracted in the \mathbf{k}_d direction carries information on the Fourier transform of the permittivity for all spatial frequencies. More precisely, by iterating the Born series, it is shown that the second order of $\mathbf{E}(\mathbf{k}_d, \mathbf{k})$ can be cast in the form $\int \mathbf{B}(\mathbf{k}_d, \mathbf{k}, \mathbf{k}') \tilde{\Delta\varepsilon}(\mathbf{k}_d - \mathbf{k}') \tilde{\Delta\varepsilon}(\mathbf{k}' - \mathbf{k}) d\mathbf{k}'$.³² Thus, it should be possible to obtain a better resolution than that classically expected from considerations of the single-scattering approximation. Note that the presence of multiple scatter-

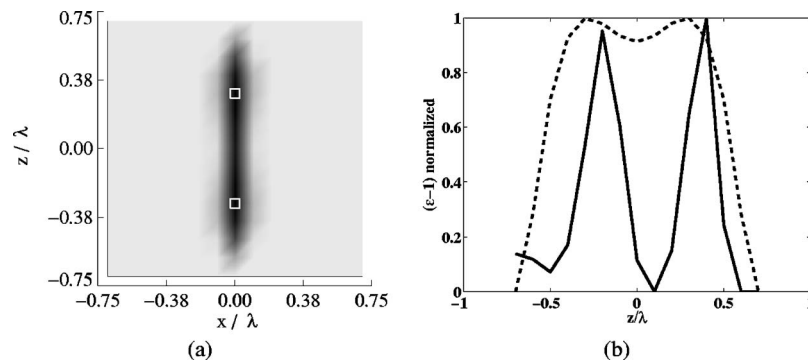


Fig. 3. (a) Map in the $y=0$ plane of the reconstructed permittivity of two dipoles (cubes of width $\lambda/20$, $\varepsilon=2.25$) separated by 0.6λ along the z axis. (b) Normalized reconstructed permittivity contrast $[(\varepsilon-1)/\max(\varepsilon-1)]$ versus z/λ for $x=y=0$: dashed curve, two dipoles separated by 0.6λ along the z axis; solid curve, two cubes of width $\lambda/4$, $\varepsilon=2.25$, whose centers are separated by the same distance as the dipoles, 0.6λ , along the z axis.

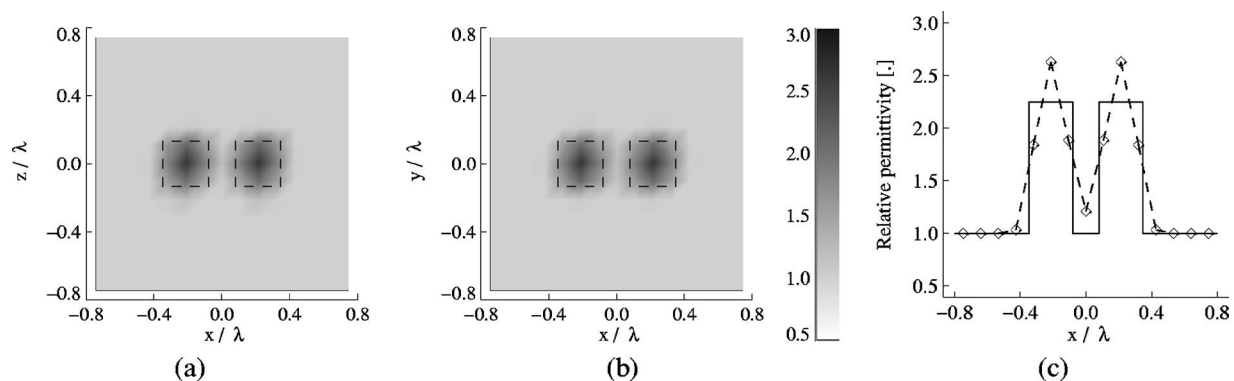


Fig. 4. Two cubes of side $a=\lambda/4$ separated by a distance $c=\lambda/7$ along the x axis. (a) and (b) show reconstructed maps of permittivities with a test domain of size $(1.6 \times 1.6 \times 1.6) \lambda^3$; the square in dashed line indicates the position of the actual cubes: (a) map of the relative permittivity in the plane (x,z) for $y=0$; (b) map of the relative permittivity in the plane (x,y) for $z=0$. (c) Relative permittivity versus x for $y=z=0$ (dashed curve) and the actual profile (solid curve).

ing is linked to the size of the objects and to their dielectric contrast. Thus, it is to be expected that the power of resolution of a nonlinear imaging system depends on these two parameters. This will be confirmed in Subsection 3.B.

B. Spatial Separation of Two Scatterers

To check the resolution along the x axis or z axis, we have taken two cubes of side $a=\lambda/4$ and permittivity $\varepsilon=2.25$ that are placed either along the x axis and separated by a distance $c=\lambda/7$ or along the z axis and separated by a distance $c=\lambda/3$ (the centers of the cubes are separated by $c+\lambda/4$).

We have first tried the linear inversion scheme presented in Ref. 6, which is based on the reconstruction of the induced dipoles inside the test domain. Even with a posttreatment, the method failed to distinguish the two cubes, either in the x or z directions. We have also checked an inversion procedure based on the extended Born approximation. This approximation yields a better estimation of the internal electric field than the standard Born approximation, Ref. 33, and it permits one to skip the resolution of Eq. (8) during the iterative process. This method allowed us to resolve the two objects placed along the x axis, though with an estimation of the relative per-

mittivity significantly smaller than the actual one, but failed in resolving the two cubes placed along the z axis.

On the other hand, the full nonlinear scheme was successful in retrieving accurately the location, permittivity, and size of the cubes in both configurations, as can be seen in the views of the reconstructed permittivity maps in the (x,y) and (x,z) planes, Figs. 4 and 5. Not surprising, when multiple scattering is present a nonlinear inversion scheme is more efficient than a linear one. The slight shift of the positions of the cubes in Fig. 5 along the positive z axis can possibly be explained by the nonsymmetric configuration of the illumination and collection and the shadowing effect between the cubes. This shift vanishes when the illumination is symmetric with respect to the (x,y) plane, or when the separation of the cubes is increased.

We now check the influence of the permittivity of the objects on the reconstruction. In Figs. 6(a)–6(c) we plot the reconstructed permittivity versus z/λ for $x=y=0$ of two cubes of width $\lambda/4$ separated by $c=\lambda/3$ along the z axis, with permittivities $\varepsilon=1.01$, 2.25 , and 4 , respectively. We first observe that the retrieved value of the permittivity is correct in the three cases. This shows that our imaging system permits the characterization of the sample. Second, we find, as expected, that the greater the permittivity, the better the resolution of the two cubes. In par-

ticular, when $\varepsilon=1.01$, the Born approximation is valid and the inversion scheme fails to resolve the two cubes. In our opinion, this example emphasizes the role of multiple scattering in the resolution.

C. Robustness against Noise

In this section we analyze the robustness of our inversion algorithm with respect to different kinds of noise. First, the scattered far-field data, $\mathbf{f}_{l=1,\dots,L}$, are corrupted with uncorrelated noise on each component of the electric field, and for each observation point

$$\operatorname{Re}[\tilde{f}_{l,v}(\mathbf{r}_k)] = \operatorname{Re}[f_{l,v}(\mathbf{r}_k)] + uA_r\xi_{l,v}, \quad (15)$$

$$\operatorname{Im}[\tilde{f}_{l,v}(\mathbf{r}_k)] = \operatorname{Im}[f_{l,v}(\mathbf{r}_k)] + uA_i\eta_{l,v}, \quad (16)$$

where v stands for the component along x , y , or z . $\xi_{l,v}$ and $\eta_{l,v}$ are random numbers with uniform probability density in $[-1, 1]$, and u is a real number smaller than unity that monitors the noise level:

$$A_r = \max\{\operatorname{Re}(f_{l,v})\} - \min\{\operatorname{Re}(f_{l,v})\}_{l=1,\dots,L;v},$$

$$A_i = \max\{\operatorname{Im}(f_{l,v})\} - \min\{\operatorname{Im}(f_{l,v})\}_{l=1,\dots,L;v}.$$

Figure 7 shows the effect of noise on the reconstructed maps of relative permittivity versus the noise level u . The reconstructed objects are always perfectly localized in

both planes (x, z) and (x, y) whatever the value of u [5% or 15%; see Figs. 7(a), 7(b), 7(d), and 7(e)]. The separation between the two cubes is still visible, the only effect of the uncorrelated noise being an increase of the relative permittivity. As shown in Figs. 7(c) and 7(f), when u increases, the maximum of the relative permittivity increases. In fact, in the case presented A_r and A_i are both positive, hence the intensity of the noisy scattered field, averaged over the observation domain Γ , is larger than the intensity of the uncorrupted field. In our opinion the consequence is a larger relative permittivity in the reconstruction to counterbalance the increase in this intensity.

The previous noise was uncorrelated but it is most likely that experimental noise will be correlated. Indeed, because of the envisaged experimental setup, we have suspected cumulative errors on the phase measurements as one moves away from the specular direction. Hence, to be faithful to the experimental setup, we have chosen a correlated noise of the form

$$\tilde{f}_{l,v}(\mathbf{r}_k) = f_{l,v}(\mathbf{r}_k)e^{i\psi_{l,v}}, \quad \psi_{l,v} = \psi_{l,v}^g + \psi_{l,v}^a, \quad (17)$$

where v denotes the component x , y , or z ; $l=1, \dots, L$; and $k=1, \dots, M$. $\psi_{l,v}^g$ is a Gaussian noise with mean 0 and standard deviation σ while $\psi_{l,v}^a$ is a correlated noise defined as $\psi_{l,v}^a = |\mathbf{k}_d - \mathbf{k}|/|\mathbf{k}|\gamma/2$. In the experimental configura-

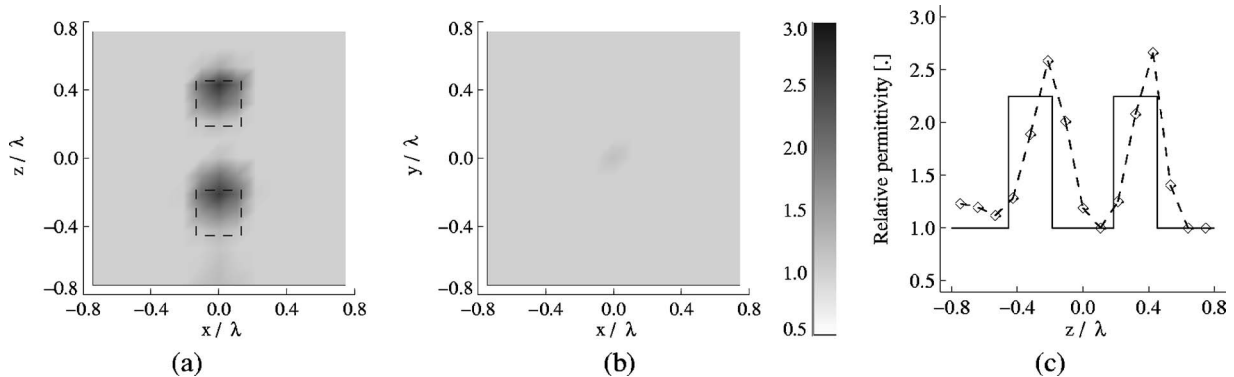


Fig. 5. Two cubes of size $a=\lambda/4$ separated by a distance $c=\lambda/3$ along the z axis. (a) and (b) show reconstructed maps of permittivities for a test domain Ω sized $(1.6 \times 1.6 \times 1.6)\lambda^3$; the square in dashed line indicates the position of the actual cubes: (a) map of the relative permittivity in the plane (x, z) for $y=0$; (b) map of the relative permittivity in the plane (x, y) for $z=0$. (c) Comparison between the reconstructed relative permittivity (dashed curve) and the actual profile (solid curve) versus z for $x=y=0$.

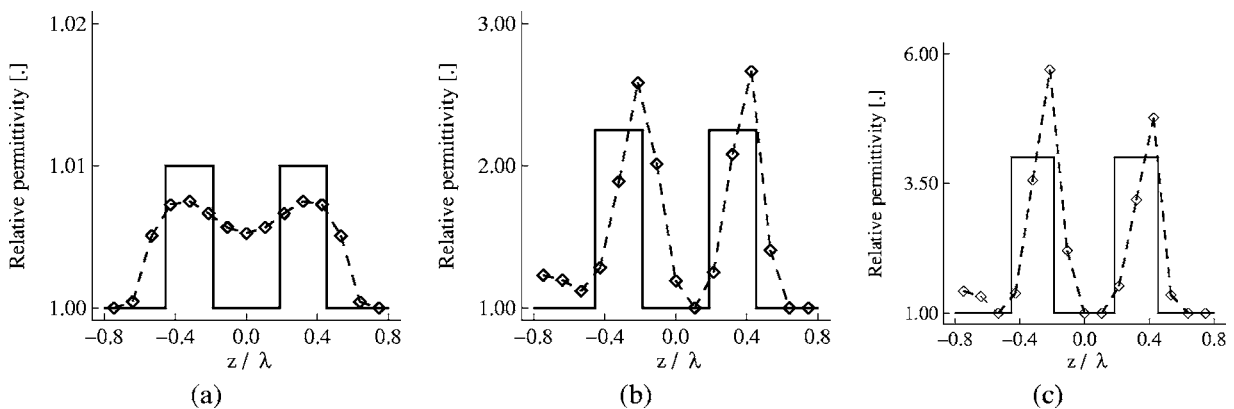


Fig. 6. Two cubes of side $a=\lambda/4$ separated by a distance $c=\lambda/3$ along the z axis for different permittivities. We display the permittivity versus z/λ for $x=y=0$. In solid is the actual profile, in dashed curve with diamond symbols, the reconstruction obtained with the non-linear inversion scheme. The actual permittivity of the two cubes is ε (a) 1.01, (b) 2.25, (c) 4.0.

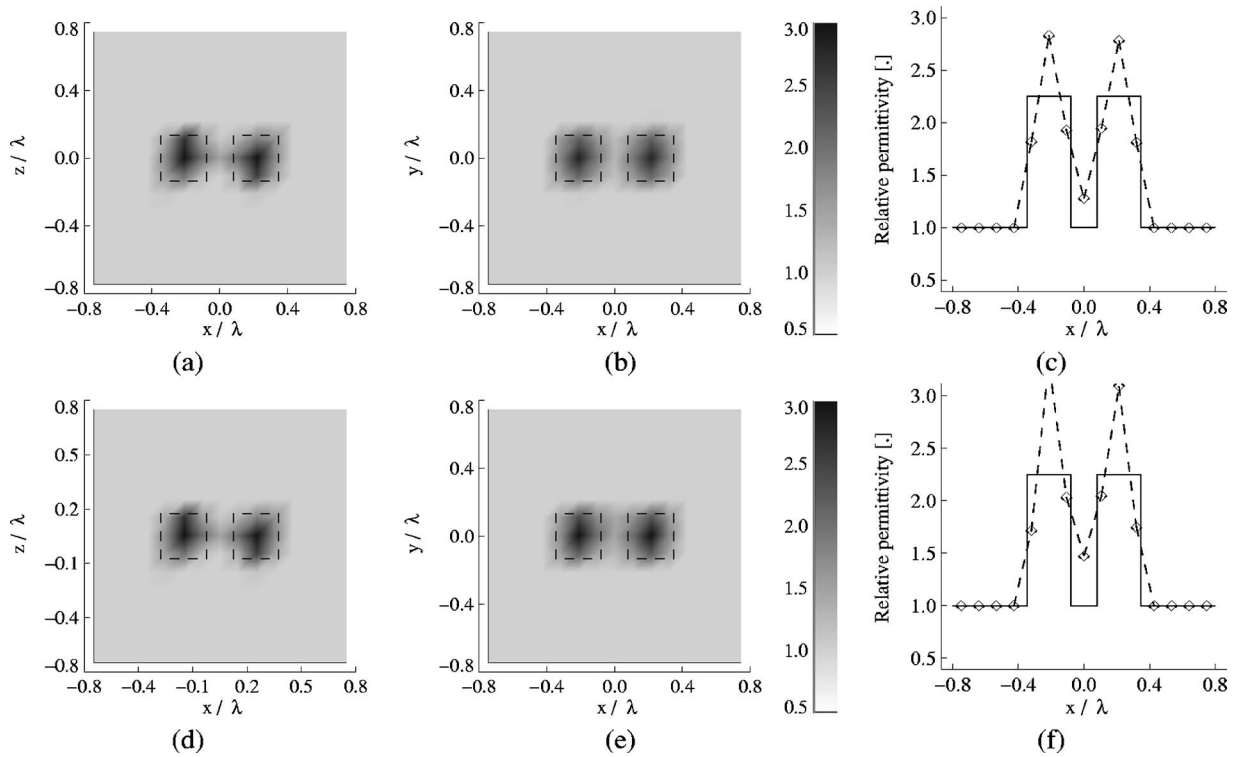


Fig. 7. The objects are the same as those in Fig. 4, and we have kept the same representation, but with uncorrelated noise on the scattered field. The upper figures (a), (b), (c) are obtained for a level of noise $u=5\%$, the lower figures (d), (e), (f) for a stronger noise $u=15\%$.

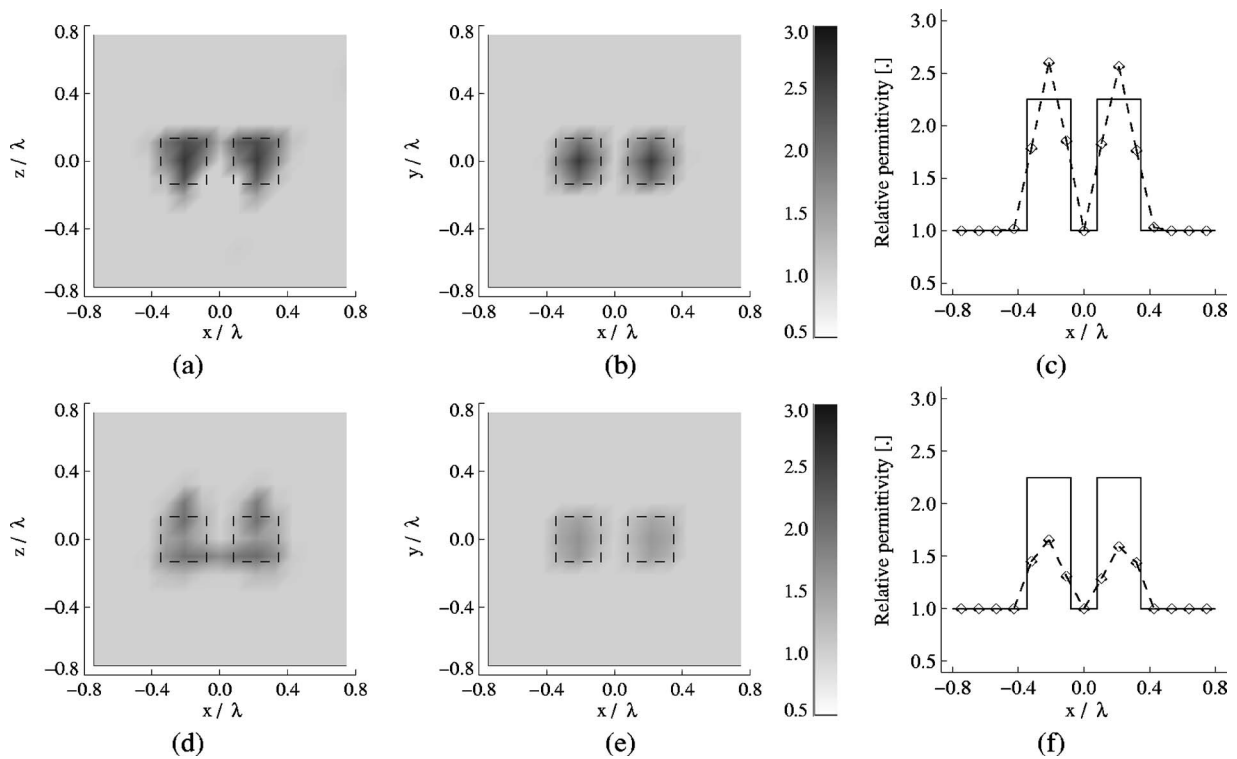


Fig. 8. Same as Fig. 7 but the noise consists now of multiplying the scattered field by a phase factor of the form $e^{i\psi}$ as specified in Eq. (17). The term of Gaussian noise is of a standard deviation $\sigma=5^\circ$, and for the correlated phase ψ^a we have chosen $|\gamma|=10^\circ$. For the upper figures $\gamma=10^\circ$, for the lower figures, $\gamma=-10^\circ$.

ration, Fig. 1, the most important error on the phase, $\max(\psi^a) \approx \gamma$, occurs when $k_{d,x} = -k_{x,y}$ or $k_{d,y} = -k_{y,z}$, and the maximum angle of incidence is $\theta^{\text{inc}} = \pm 80^\circ$.

We note that the correlated noise, Fig. 8, has more impact than the uncorrelated one on the reconstructed map of permittivity. In the (x,y) plane, the localization, size, and value of permittivity are still accurate [Figs. 8(b) and 8(e)]. The two cubes are resolved without any doubt since the reconstructed relative permittivity vanishes between them as shown in Figs. 8(c) and 8(f). The main changes appear in the (x,z) plane where we observe a shift of the center of the cubes along the z axis. We note that the shift is different, following the sign of γ . If γ is positive (negative) the reconstructed cubes are shifted in the direction of negative (positive) z . In fact, when γ is positive the phase factor ψ^a is also positive.

With our model, the maximum error on the phase occurs for the scattered fields far from the specular direction, i.e., for the data richest in information on the position of the objects. For the scattered field far from the specular direction, the added phase ψ^a can be interpreted as an increase of the optical path. Since the points of observation are above the plane (x,y) the phase error yields a shift of the objects in the direction of negative z . Conversely, when γ is negative the error on the phase translates the two cubes in the direction of positive z . One notes that whereas for $\gamma > 0$ the value of the relative permittivity is close to the actual one, this is not the case for $\gamma < 0$: The reconstructed relative permittivity is weaker. Unfortunately, we did not find a complete explanation of the underestimation of the permittivity when $\gamma < 0$. How-

ever, it is obvious that the two values of γ cannot lead to the same result. This is due to the nonsymmetrical measurement configuration: The illumination and the observation points are located on opposite sides of the (x,y) plane.

D. Multiple Scatterers

In the previous cases, we considered a simple target made of only two cubes. The number of data was $65 \times 16 = 1040$ (this number should be multiplied by a factor of 2 since we are considering the complex amplitude of the

Table 1. Coordinates of the Center of the Nine Cubes ($a = \lambda/4$) Embedded in an Investigation Domain Ω of Volume $8\lambda^3$ ^a

Scatterer	Coordinates			Relative Permittivity	
	x/λ	y/λ	z/λ	Fig. 9	Fig. 10
1	-0.575	-0.375	-0.675	2.25	1.5
2	0.675	-0.375	-0.675	2.25	1.5
3	-0.325	-0.375	-0.425	2.25	2.25
4	0.675	-0.375	-0.075	2.25	1.5
5	-0.575	-0.375	0.575	2.25	2.25
6	-0.175	-0.375	0.575	2.25	2.25
7	0.575	-0.375	0.575	2.25	2.25
8	-0.325	0.575	-0.425	2.25	1.5
9	0.675	0.575	-0.075	2.25	2.25

^aMaps of the reconstructed relative permittivity by our nonlinear inversion algorithm are presented in Figs. 9 and 10.

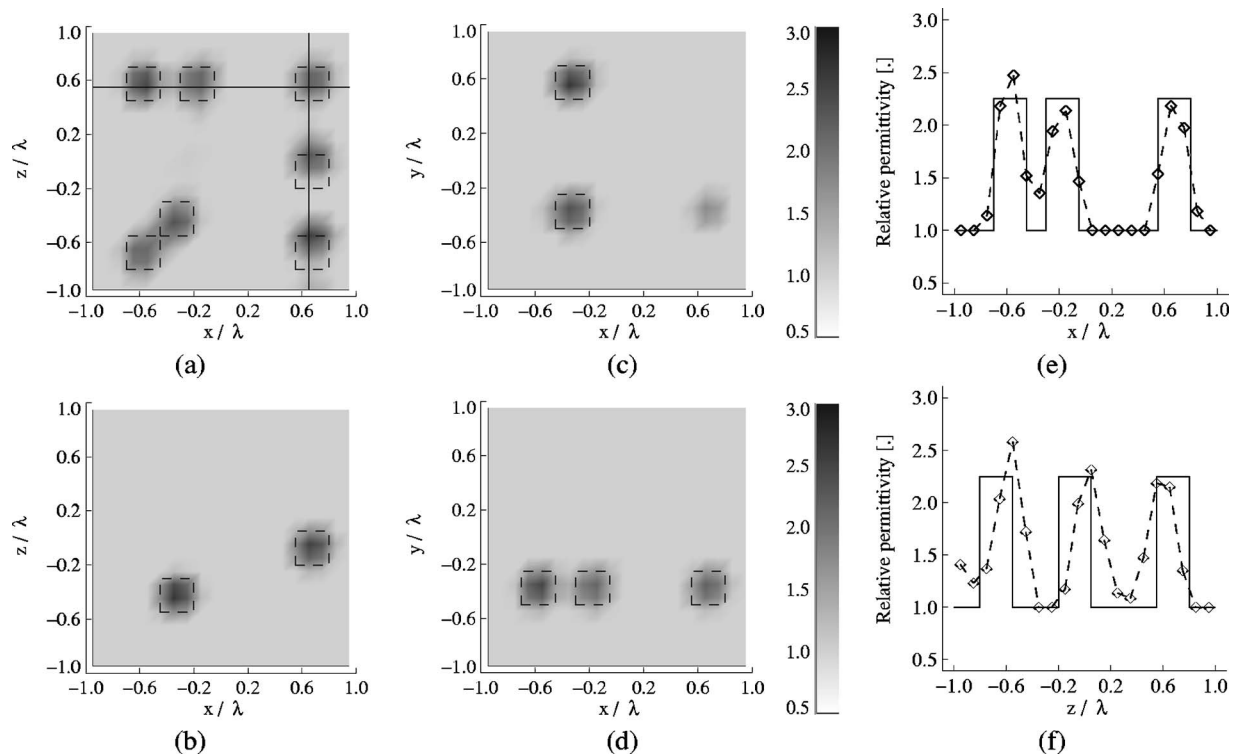


Fig. 9. Nine cubes of side $a = \lambda/4$ distributed in a test domain of volume $8\lambda^3$ (see Table 1 for their positions). (a), (b), (c), (d) are the reconstructed maps of the relative permittivities: (a) map in the (x,z) plane for $y/\lambda = -0.375$, (b) map in the (x,z) plane for $y/\lambda = 0.575$, (c) map in the (x,y) plane for $z/\lambda = -0.675$, (d) map in the (x,y) plane for $z/\lambda = 0.575$. (e) Relative permittivity versus x/λ along the horizontal line plotted in (a). (f) Relative permittivity versus z/λ along the vertical line plotted in (a).

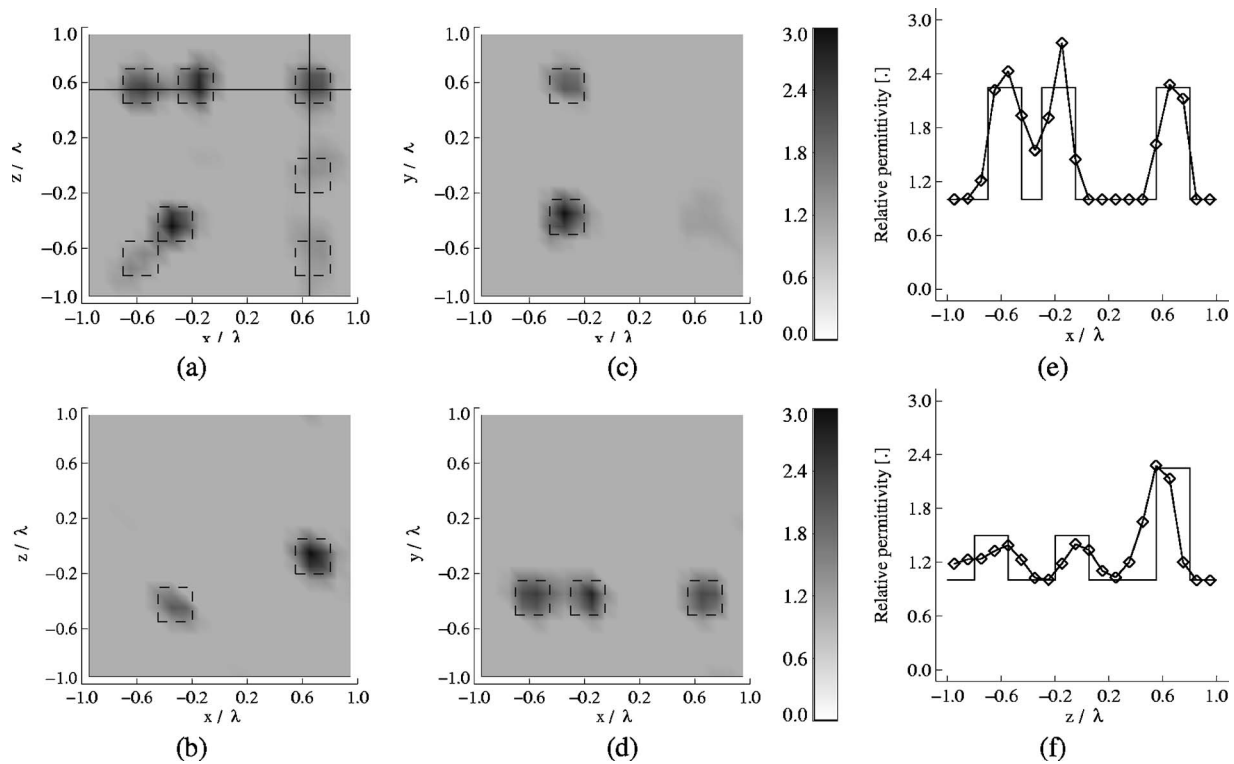


Fig. 10. Same as Fig. 9 but the cubes have different relative permittivities as detailed in Table 1.

electric field) while that of the unknowns, i.e., the polarizability of each cell, was about 3375. Hence, the number of measurements and unknowns were close to each other and, finally, only few polarizabilities departed from that of the background medium. One can wonder what would happen if the test domain were larger, with several objects, and the number of unknowns larger than that of the measurements. Hence, in the last example, we consider an investigation domain Ω of side 2λ ($V=8\lambda^3$) which yields 8000 unknowns (note that if the relative permittivity were complex the number of unknowns would be multiplied by a factor of 2) while the number of data remains equal to 1040. The sample consists of nine cubes of side $a=\lambda/4$, distributed in the box Ω as specified in Table 1.

Figure 9 shows, in different planes, comparisons between the reconstructed relative permittivities and the actual ones. One can note that, even with many objects and a number of unknowns larger than the number of measurements, the reconstructed maps localize without any doubt the positions of the objects [see Figs. 9(a)–9(d)]. Satisfactory reconstructed profiles have been obtained. These profiles are plotted in dashed curves in Figs. 9(e) and 9(f), which show also that the presence of many objects does not alter the power of resolution along the x or z axis. The two cubes that are separated by a distance of $\lambda/7$ along the x axis (cubes 5 and 6 of Table 1) and the two cubes separated by $\lambda/3$ along the z axis (cubes 2 and 4) are accurately resolved. In Fig. 9(f) one can notice the same shift along the z axis as that observed in Fig. 5.

The nonlinear scheme is also able to characterize unknown objects by giving a correct estimation of their permittivity. In Fig. 10 we plot the map of permittivity of a target made of several cubes placed at the same positions as in Fig. 9 but presenting different permittivities (see

Table 1). The scattered far-field data are corrupted with the uncorrelated noise described in Eqs. (15) and (16) with $u=5\%$. We observe that the location, size, and permittivity of each cube are accurately retrieved. We have also checked the robustness of the reconstruction to correlated noise, Eq. (17), and obtained satisfactory results.

4. CONCLUSION

We have proposed a three-dimensional nonlinear inversion scheme that permits one to retrieve the map of permittivity of unknown objects from their scattered far field in an optical diffraction tomography experiment in transmission. The efficiency of the algorithm, based on the coupled-dipole method, has been checked successfully on complex targets made of many cubes positioned on various planes of a box. We have shown that, for objects small compared to the wavelength and with moderate dielectric constant, accounting for multiple scattering in the reconstruction procedure improves the image significantly. Moreover, we have pointed out that the presence of multiple scattering permits one to obtain a power of resolution beyond that classically expected. Moreover, our algorithm is robust to both correlated and uncorrelated noise. Last, our method can be extended without conceptual difficulties to configurations that are closer to realistic experiments, for example, objects deposited on a known substrate or buried inside a semi-infinite medium. This can be done by adding to the tensor of the free-space field susceptibility the tensor of the environment.^{34–36}

ACKNOWLEDGMENTS

This work was supported by a grant of the Ministère de la Recherche, ACI 02 2 0225, and the Conseil Général des

Bouches du Rhône and the Conseil Régional PACA. The authors thank Frédéric Forestier for the computer science support. Kamal Belkebir's e-mail address is kamal.belkebir@fresnel.fr.

REFERENCES

- V. Lauer, "New approach to optical diffraction tomography yielding a vector equation of diffraction tomography and a novel tomographic microscope," *J. Microsc.* **205**, 165–176 (2002).
- N. Destouches, C. A. Guérin, M. Lequime, and H. Giovannini, "Determination of the phase of the diffracted field in the optical domain. Application to the reconstruction of surface profiles," *Opt. Commun.* **198**, 233–239 (2001).
- E. Wolf, "Three-dimensional structure determination of semi-transparent objects from holographic data," *Opt. Commun.* **1**, 153–156 (1969).
- S. Kawata, O. Nakamura, and S. Minami, "Optical microscope tomography. I. Support constraint," *J. Opt. Soc. Am. A* **4**, 292–297 (1987).
- P. S. Carney and J. C. Schotland, "Three-dimensional total-internal reflection microscopy," *Opt. Lett.* **26**, 1072–1074 (2001).
- P. Chaumet, K. Belkebir, and A. Sentenac, "Three-dimensional subwavelength optical imaging using the coupled dipole method," *Phys. Rev. B* **69**, 245405 (2004).
- E. M. Purcell and C. R. Pennypacker, "Scattering and absorption of light by nonspherical dielectric grains," *Astrophys. J.* **186**, 705–714 (1973).
- J. D. Jackson, *Classical Electrodynamics*, 2nd ed. (Wiley, 1975).
- A. Lakhtakia, "Strong and weak forms of the method of moments and the coupled dipole method for scattering of time-harmonic electromagnetic fields," *Int. J. Mod. Phys. C* **3**, 583–603 (1992).
- P. C. Chaumet and M. Nieto-Vesperinas, "Coupled dipole method determination of the electromagnetic force on a particle over a flat dielectric substrate," *Phys. Rev. B* **61**, 14119–14127 (2000).
- P. C. Chaumet and M. Nieto-Vesperinas, "Electromagnetic force on a metallic particle in the presence of a dielectric surface," *Phys. Rev. B* **62**, 11185–11191 (2000).
- P. C. Chaumet and M. Nieto-Vesperinas, "Time-averaged total force on a dipolar sphere in an electromagnetic field," *Opt. Lett.* **25**, 1065–1067 (2000).
- B. T. Draine, "The discrete dipole approximation and its application to interstellar graphite grains," *Astrophys. J.* **333**, 848–872 (1988).
- W. C. Chew and Y. M. Wang, "Reconstruction of two-dimensional permittivity distribution using the distorted wave Born iterative method," *IEEE Trans. Med. Imaging* **9**, 218–235 (1990).
- N. Joachimowicz, C. Pichot, and J.-P. Hugonin, "Inverse scattering: An iterative numerical method for electromagnetic imaging," *IEEE Trans. Antennas Propag.* **39**, 1742–1751 (1991).
- A. G. Tijhuis, "Born-type reconstruction of material parameters of an inhomogeneous, lossy dielectric slab from reflected-field data," *Wave Motion* **11**, 151–173 (1989).
- A. G. Tijhuis, K. Belkebir, A. C. S. Litman, and B. P. de Hon, "Theoretical and computational aspects of 2-D inverse profiling," *IEEE Trans. Geosci. Remote Sens.* **GE-39**, 1316–1330 (2001).
- R. E. Kleinman and P. M. van den Berg, "A modified gradient method for two-dimensional problems in tomography," *J. Comput. Appl. Math.* **42**, 17–35 (1992).
- R. E. Kleinman and P. M. van den Berg, "An extended range-modified gradient technique for profile inversion," *Radio Sci.* **28**, 877–884 (1993).
- K. Belkebir and A. G. Tijhuis, "Modified² gradient method and modified Born method for solving a two-dimensional inverse scattering problem," *Inverse Probl.* **17**, 1671–1688 (2001).
- K. Belkebir, S. Bonnard, F. Pezin, P. Sabouroux, and M. Saillard, "Validation of 2D inverse scattering algorithms from multi-frequency experimental data," *J. Electromagn. Waves Appl.* **14**, 1637–1667 (2000).
- K. Belkebir and A. Sentenac, "High resolution optical diffraction microscopy," *J. Opt. Soc. Am. A* **20**, 1223–1229 (2003).
- P. S. Carney, V. A. Markel, and J. C. Schotland, "Near-field tomography without phase retrieval," *Phys. Rev. Lett.* **86**, 5874–5877 (2001).
- P. M. van den Berg and R. E. Kleinman, "A contrast source inversion method," *Inverse Probl.* **13**, 1607–1620 (1997).
- A. Abubakar, P. M. van den Berg, and B. J. Kooij, "A conjugate gradient contrast source technique for 3D profile inversion," *IEICE Trans. Electron.* **E83-C**, 1864–1874 (2000).
- A. Abubakar and P. M. van den Berg, "The contrast source inversion method for location and shape reconstructions," *Inverse Probl.* **18**, 495–510 (2002).
- W. H. Press, B. P. Flannery, S. A. Teukolski, and W. T. Vetterling, *Numerical Recipes: The Art of Scientific Computing* (Cambridge U. Press, 1986).
- K. Belkebir, R. E. Kleinman, and C. Pichot, "Microwave imaging—Location and shape reconstruction from multifrequency scattering data," *IEEE Trans. Microwave Theory Tech.* **45**, 469–476 (1997).
- L. Souriau, B. Duchêne, D. Lesselier, and R. E. Kleinman, "Modified gradient approach to inverse scattering for binary objects in stratified media," *Inverse Probl.* **12**, 463–481 (1996).
- R. E. Kleinman and P. M. van den Berg, "Two-dimensional location and shape reconstruction," *Radio Sci.* **29**, 1157–1169 (1994).
- J. Daillant and A. Gibaud, *X-Ray and Neutron Reflectivity Lecture Notes in Physics* (Springer-Verlag, 1999), p. 130.
- C.-A. Guérin and A. Sentenac, "Second-order perturbation theory for scattering from heterogeneous rough surfaces," *J. Opt. Soc. Am. A* **21**, 1251–1260 (2004).
- T. M. Habashy, R. W. Groom, and B. R. Spies, "Beyond the Born and Rytov approximations—A nonlinear approach to electromagnetic scattering," *J. Geophys. Res., [Solid Earth]* **98**, 1759–1775 (1993).
- P. C. Chaumet, A. Rahmani, F. de Fornel, and J.-P. Dufour, "Evanescent light scattering: The validity of the dipole approximation," *Phys. Rev. B* **58**, 2310–2315 (1998).
- A. Rahmani, P. C. Chaumet, and F. de Fornel, "Environment-induced modification of spontaneous emission: Single-molecule near-field probe," *Phys. Rev. A* **63**, 023819 (2001).
- P. C. Chaumet, A. Rahmani, and G. W. Bryant, "Generalization of the coupled dipole method to periodic structure," *Phys. Rev. B* **67**, 165404 (2003).